

Electrical and thermal transport properties of the electron-doped cuprate $\text{Sm}_{2-x}\text{Ce}_x\text{CuO}_{4-y}$ system

D J Scanderbeg¹, B J Taylor², R E Baumbach³, J Paglione⁴ and M B Maple

Department of Physics, University of California, San Diego, La Jolla, CA 92093, USA

E-mail: dscanderbeg@ucsd.edu, benjamin.taylor4@navy.mil, baumbach@magnet.fsu.edu, paglione@umd.edu and mbmaple@ucsd.edu

Received 9 May 2016, revised 15 July 2016

Accepted for publication 14 September 2016

Published 5 October 2016



Abstract

Electrical and thermal transport measurements were performed on thin films of the electron-doped superconductor $\text{Sm}_{2-x}\text{Ce}_x\text{CuO}_{4-y}$ ($x = 0.13 - 0.19$) in order to study the evolving nature of the charge carriers from the under-doped to over-doped regime. A temperature versus cerium content ($T - x$) phase diagram has been constructed from the electrical transport measurements, yielding a superconducting region similar to that found for other electron-doped superconductors. Thermopower measurements show a dramatic change from the underdoped region ($x < 0.15$) to the overdoped region ($x > 0.15$). Application of the Fisher–Fisher–Huse (FFH) vortex glass scaling model to the magnetoresistance data was found to be insufficient to describe the data in the region of the vortex-solid to vortex-liquid transition. It was found instead that the modified vortex glass scaling model of Rydh, Rapp, and Anderson provided a good description of the data, indicating the importance of the applied field on the pinning landscape. A magnetic field versus temperature ($H - T$) phase diagram has also been constructed for the films with $x \geq 0.14$, displaying the evolution of the vortex glass melting lines $H_g(T)$ across the superconducting regime.

Keywords: electron doped, high T_c cuprate, vortex dynamics

(Some figures may appear in colour only in the online journal)

1. Introduction

Establishing a complete $H - T - x$ phase diagram of both hole- and electron-doped high- T_c cuprates is an important step towards building an understanding of the physical origin of superconductivity in these compounds. An immense volume of work has been carried out in this regard for hole-doped cuprates since their discovery almost 30 years ago.

¹ Present Address: Department of Radiation Oncology, UC San Diego, La Jolla, CA 92093, USA

² Present Address: Space and Naval Warfare Systems Center—Pacific, San Diego, CA 92152, USA

³ Present Address: National High Magnetic Field Laboratory, Florida State University, 1800 E. Paul Dirac Dr, Tallahassee, FL 32310, USA

⁴ Present Address: Center for Nanophysics and Advanced Materials, Department of Physics, University of Maryland, College Park, MD 20742, USA

However, it has been only in the last decade that the electron-doped cuprates have begun to receive similar levels of attention experimentally. Of the class of electron-doped cuprate superconductors having the composition of $R_{2-x}\text{Ce}_x\text{CuO}_{4\pm\delta}$ ($R = \text{La, Pr, Nd, Sm, and Eu}$), the compounds which received the most attention over the past two decades have been $\text{La}_{2-x}\text{Ce}_x\text{CuO}_{4-y}$, $\text{Nd}_{2-x}\text{Ce}_x\text{CuO}_{4-y}$, and $\text{Pr}_{2-x}\text{Ce}_x\text{CuO}_{4-y}$ [1–7]. The remaining $R_{2-x}\text{Ce}_x\text{CuO}_{4\pm\delta}$ compounds have seen a recent increase of attention, particularly $\text{Sm}_{2-x}\text{Ce}_x\text{CuO}_{4-y}$, with the mapping of the $T_c - x$ phase diagram [8], investigation of the pseudogap phase [9–11], measurements of the superconducting gap energy [12], and experimental and theoretical investigation of the Fermi surface [13, 14].

This recent work has been primarily concerned with the evolution of the physical properties of $\text{Sm}_{2-x}\text{Ce}_x\text{CuO}_{4-y}$ as a function of Ce content, i.e. the mapping of the $T - x$ phase

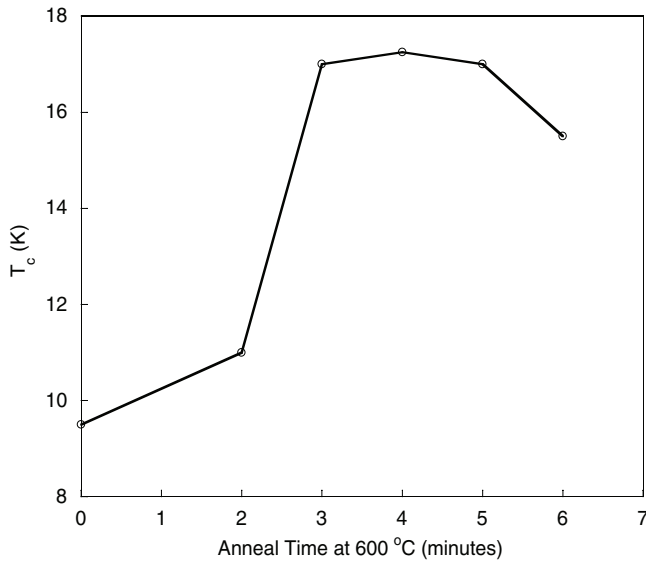


Figure 1. Superconducting critical temperature T_c versus anneal (dwell) time at 600 °C for the $x = 0.16$ samples. An optimal anneal time of 4 min was also found for all other concentrations grown.

diagram. There remains, at least, the need to extend investigation of key properties along the ‘ H -axis’, i.e. to complete the $H - T - x$ phase diagram. Furthermore, the Sm^{3+} ions in $\text{Sm}_{2-x}\text{Ce}_x\text{CuO}_{4-y}$ order antiferromagnetically below the Néel temperature $T_N \sim 6\text{K}$ into an arrangement that is unique in high- T_c materials, wherein the magnetic moment of the Sm^{3+} sites align within a single ab plane ferromagnetically, but each adjacent plane along the c -axis is aligned antiferromagnetically [15]. This presents an opportunity to both investigate the interplay of superconductivity and magnetism and the possible role of magnetic excitations in the pairing process [16, 17], and, also to study of the effect of magnetic order on the dynamic properties of vortices in the region of the melting of the vortex solid.

We report here electrical and thermal transport measurements on thin films of $\text{Sm}_{2-x}\text{Ce}_x\text{CuO}_{4-y}$ ($x = 0.13\text{--}0.19$) in order to study the progression of key physical properties from the under-doped to over-doped regime. We find similar features in the evolution of thermopower properties as that found for films of $\text{Pr}_{2-x}\text{Ce}_x\text{CuO}_{4-y}$ [18], which have been taken as evidence for the presence of both holes and electrons as charge carriers. From high magnetic field ab -plane resistivity $\rho(T)$ measurements, we find a temperature T^* for each sample below which a T -linear component and/or negative magnetoresistivity in $\rho(T)$ can be extracted. The value of T^* is correlated here with a broad feature in the derivative of the thermopower data, dS/dT . The value of T^* decreases linearly with x across the under-doped to over-doped regime in a manner similar to the pseudo-gap temperature that is observed in hole-doped cuprates [19–21], which is also associated with the formation of a T -linear component in $\rho(T)$ [22]. While we associate the values of T^* obtained here as the pseudogap temperature, we note, however, that the presence of a pseudogap in the electron doped cuprates remains an open issue [23–26]. Finally, from an analysis of the vortex glass melting transition we find that the pinning landscape in the $H - T$ plane of $\text{Sm}_{2-x}\text{Ce}_x\text{CuO}_{4-y}$

is significantly affected by the application of the magnetic field.

2. Experimental details

Polycrystalline $\text{Sm}_{2-x}\text{Ce}_x\text{CuO}_{4-y}$ target material for use in the pulsed laser deposition (PLD) process was formed by a solid state reaction technique with starting materials of 99.99% pure oxides of Sm_2O_3 , the dopant CeO_2 , and CuO . To insure the proper stoichiometry of the target, the powders were dried in air inside alumina crucibles at 900 °C for $\geq 12\text{h}$ since both compounds are known to absorb water readily [27]. Once dry, the starting materials were weighed and mixed in an ultra-high purity (UHP) Ar atmosphere. The prepared mixture was fired in air for $\geq 18\text{h}$ at 900 °C in an alumina crucible, then ground by hand and re-fired in air at 1000 °C for $\geq 24\text{h}$. Subsequently, the material was ground in a centrifugal ball mill, and the resulting fine powder was pressed into a pellet and fired a final time in air at 1100 °C for $\geq 3\text{d}$. Finally, the furnace was cooled to 900 °C and the target was removed to cool in air.

The $\text{Sm}_{2-x}\text{Ce}_x\text{CuO}_{4-y}$ films were grown on yttria-stabilized zirconia (YSZ) with a (100) orientation. The optimal growth conditions of the films for each concentration of $\text{Sm}_{2-x}\text{Ce}_x\text{CuO}_{4-y}$ were determined experimentally from numerous trial growths while systematically varying the parameters including: incident laser energy density, substrate temperature, chamber pressure, and annealing conditions. The optimal incident laser energy density was determined to be $\sim 1.5\text{ J cm}^{-2}$. The energy density was verified before and after each growth using a Scientech Vector S310 external power meter. All concentrations of the films form well at $T \approx 800\text{ °C}$ and under chamber pressures of $p \approx 200\text{ mTorr}$ of flowing N_2O . The N_2O gas was flowed directly into the plume of the laser ablated material. The deposition time was 10 min in duration for all samples. After each deposition the chamber was immediately evacuated to $p < 10^{-6}$ torr and the samples were also immediately cooled to 600 °C at a rate of 20 °C min^{-1} . The samples dwelled at 600 °C for a duration of zero to 10 min, cooled again to 400 °C at a rate of 25 °C min^{-1} , dwelled for 8 min, and then the heater was shut off and the samples cooled to $\sim 100\text{ °C}$ before venting the chamber and removing the films. A plot of the superconducting critical temperature, T_c , versus anneal time is shown in figure 1 for the $x = 0.16$ sample. T_c is shown to increase with dwell time to a maximum at about 4 min. An optimal anneal time of $\approx 4\text{ min}$ at 600 °C was found for all other concentrations as well. We note that a finite ‘shelf life’ seems to be at work for all $\text{Sm}_{2-x}\text{Ce}_x\text{CuO}_{4-y}$ films grown here (and in other studies we have undertaken). Samples left exposed to the atmosphere experience a sudden rapid deterioration throughout the entire film after approximately 9–12 months—upon which the superconducting properties are irretrievably lost—leaving behind a transparent film. The shelf life of samples stored in a UHP argon atmosphere is extended to about 18 months; however the breakdown appears to be inevitable. All data presented here were taken from samples that were from 1 week

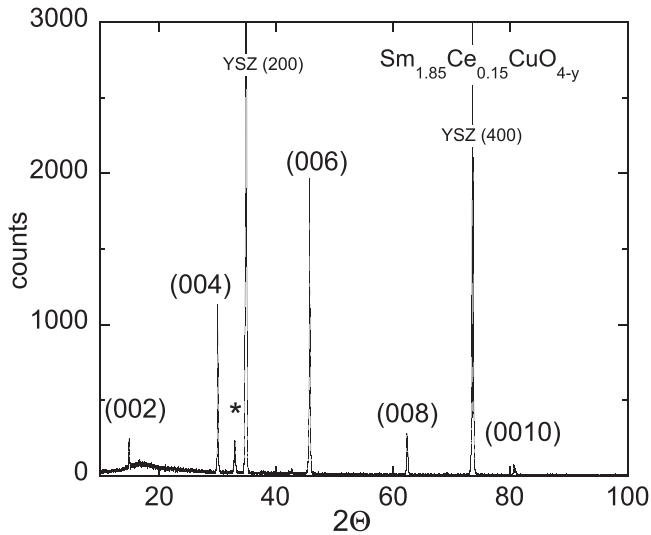


Figure 2. X-ray diffraction pattern for a $\text{Sm}_{1.85}\text{Ce}_{0.15}\text{CuO}_{4-y}$ film exhibiting the highly c -axis oriented nature of the films. An impurity peak (indicated with an asterisk) seen at $\sim 33^\circ$ is identified as CeO_2 . Other very small peaks observed are identified as being attributable to the impurity presence of either CeO_2 or Ce_2O_3 . Two substrate peaks are visible at $\sim 35^\circ$ and $\sim 73^\circ$. X-ray diffraction data for all concentrations grown indicated a similarly high quality of the films.

to 3 months old, and were stored in a ~ 1 torr vacuum in the intervening time between sample growth and measurement.

All films (including those having a non-optimal anneal time) were first characterized by x-ray diffraction and magnetization $M(T)$ measurements. Subsequently both thermal and electrical transport measurements were carried out after lithographic patterning.

Standard $\theta - 2\theta$ measurements were made using a Rigaku DMAXB x-ray diffractometer. X-ray data for the $x = 0.15$ sample is shown in figure 2. The diffraction patterns are consistent for all samples and, in addition to the substrate peaks, the major peaks are associated with the (001) reflections, indicating excellent c -axis orientation. There are two primary minor peaks consistently observed which we associate with an impurity phase. These peaks were minimized during growth optimization; however, they could never be completely removed. All of the minor peaks observed can be attributed to the presence of CeO_2 or Ce_2O_3 . In a study by Kang *et al* [28], it was suggested that, rather than being a materials processing problem, the rare earth oxide ‘impurity phase’ is actually responsible for superconductivity in the electron-doped compounds. The authors propose that, during the high temperature oxygen reducing anneal process the compound phase separates into this small Cu free ‘impurity phase’ and a ‘Cu-perfect’ $\text{Ln}_{2-x}\text{Ce}_x\text{CuO}_{4-y}$ phase. Effectively, this allows any Cu vacancies in the $\text{Ln}_{2-x}\text{Ce}_x\text{CuO}_{4-y}$ phase to be filled by the Cu atoms freed in the phase separation and creation of the Cu free R_2O_3 phase.

Magnetization $M(T)$ measurements using a quantum design MPMS were performed as part of the growth optimization process to establish T_c values. Shown in figure 3 are magnetization data for the optimally grown films having cerium concentrations $0.14 \leq x \leq 0.19$. The transition temperature T_c of the $x = 0.130$ and 0.135 samples were not determined via

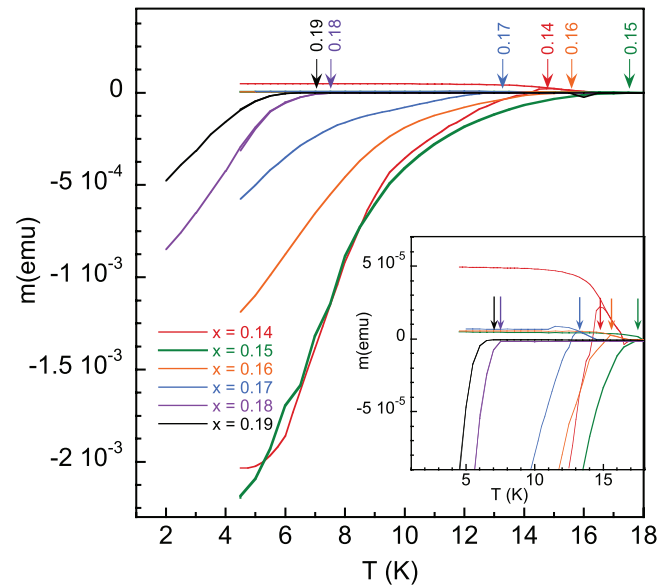


Figure 3. Magnetization $M(T)$ for the optimally oxygen-annealed $\text{Sm}_{1.85}\text{Ce}_{0.15}\text{CuO}_{4-y}$ films for the cerium concentrations $0.14 \leq x \leq 0.19$.

$M(T)$ measurements due to the ~ 2 K value. The same optimal annealing conditions as used for the $x = 0.14$ film were used for the $x = 0.130$ and 0.135 films. The same films measured in figure 3 were used for thermal and electrical transport measurements, except for $x = 0.17$ and 0.18 , for which $S(T)$ data was not obtained. Values of T_c obtained from $M(T)$ measurements were taken as the onset of the diamagnetic signal as indicated in figure 3. With the exception of the $x = 0.14$ sample, these T_c values are systematically lower than what is found below from electrical transport data. From this we conclude that the annealing of gold pads and wire leads (below) did not appreciably effect the value of T_c from the initial preparation conditions described above.

All resistivity $\rho(H, T)$ data were taken on films in which gold pads were sputtered on the as grown films in a standard 4-wire configuration. The films were annealed for 10 min in air at 500°C to allow the gold to diffuse into the films. Gold leads were attached using a two part silver epoxy and cured for 3 min at 200°C . Typical sample dimensions are $\ell \times w \times t \approx 3 \text{ mm} \times 3 \text{ mm} \times 100 \text{ nm}$. Thermopower measurements were also performed on as grown samples on a modified quantum design PPMS electrical transport puck, as described further below. Electrical transport measurements were performed with a Keithley 220 programmable current source and a Keithley 2182 nanovoltmeter with the samples in a quantum design PPMS over a temperature range $1.85 \text{ K} \leq T \leq 310 \text{ K}$ and magnetic field H range up to 9 T.

3. Experimental results

3.1. Thermopower

Similar to the Hall effect, the thermopower of a material is related to the carrier concentration and charge carrier type in a material with $S \propto 1/ne$, where n is the carrier concentration

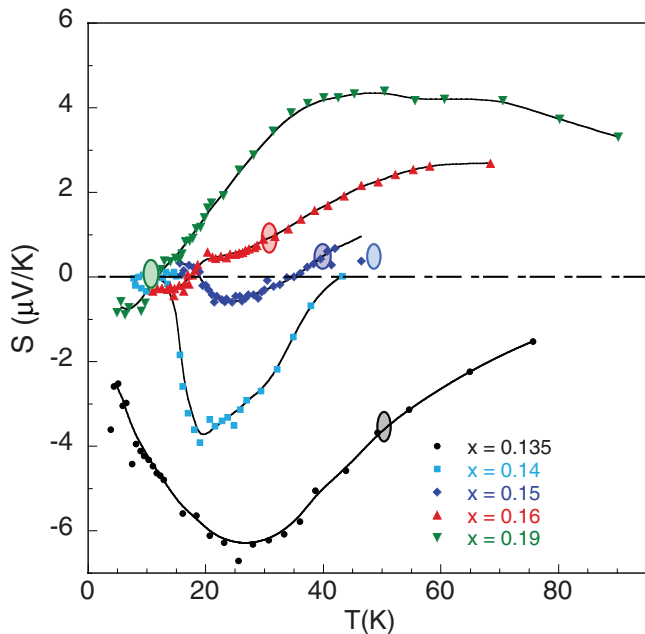


Figure 4. Thermopower data of $\text{Sm}_{2-x}\text{Ce}_x\text{CuO}_{4-y}$ films with Ce content $x = 0.135, 0.14, 0.15, 0.16,$ and 0.19 . Lines shown are smooth curve fits to the data. The shaded ovals indicate the temperatures at which a pseudo-gap is inferred from features in the resistivity data below. See also figure 5.

and e is the charge of the carrier. Thermopower measurements of high T_c cuprate materials can potentially shed light on the nature of the charge carriers in both hole-doped and electron-doped compounds and on how they evolve across the doping spectrum.

Thermopower data are shown in figure 4 for samples with cerium concentrations of $x = 0.135, 0.14, 0.15, 0.16$ and 0.19 . Smooth fit curves were applied to the data using the Kaleidagraph™ 4.5.2 package to show the general trends. It can be seen that there is a significant change in the thermopower as we move from the underdoped to the overdoped concentrations. The underdoped samples exhibit a negative thermopower whose magnitude decreases as the optimal T_c doping level ($x = 0.15$) is approached. Additionally, it is seen that the thermopower for the $x = 0.15$ sample is very small in magnitude, negative at low temperatures, and has a sign change at $T \approx 35$ K. Also indicated in figure 4 is the temperature region, T^* , for each sample below which a linear- T component in the electrical magneto-resistivity or the onset of negative magneto-resistance is observed to form. This feature is often associated with the formation of the pseudo-gap, as discussed further below in the context of the magneto-resistivity data. For further comparison to the electrical transport data, we plot in figure 5 the derivative with respect to temperature, dS/dT , calculated from the smooth curve fits to the $S(T)$ data in figure 4. With the exception of the $x = 0.135$ sample (where T_c is below the range of $S(T)$ data), the superconducting transition temperature T_c is readily correlated with the sharp downward trough ($x = 0.14, 0.15$) or upward peak ($x = 0.16, 0.19$) in the fits to the data. As in figure 4, we have also indicated the temperature region below which the linear- T resistivity component or negative magneto-resistance appears. In general, for

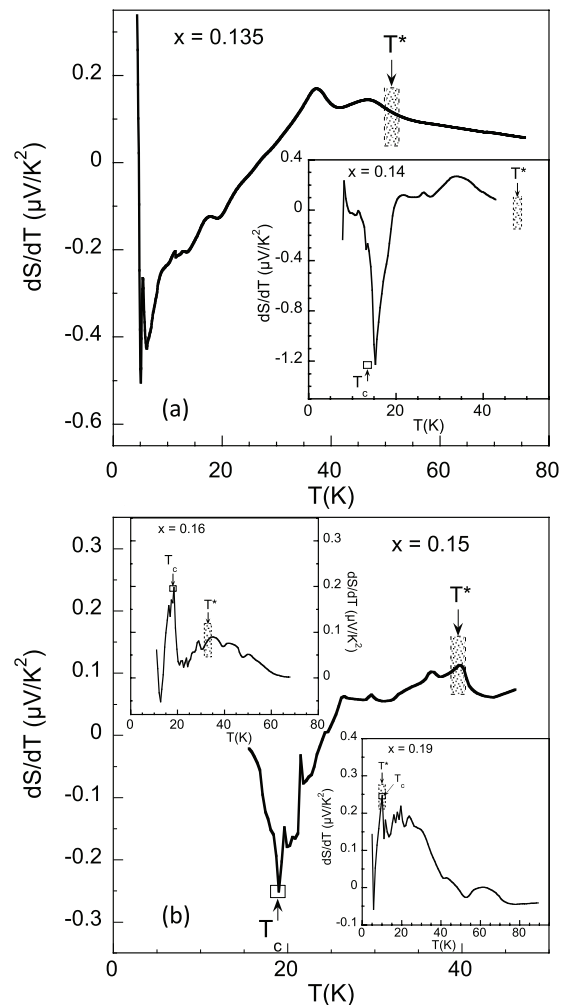


Figure 5. Change of thermopower with temperature, dS/dT , data of $\text{Sm}_{2-x}\text{Ce}_x\text{CuO}_{4-y}$ films from figure 4. (a) Under-doped samples $x = 0.135$ & 0.14 (inset). (b) Optimal ($x = 0.15$) and over-doped samples ($x = 0.16,$ & 0.19) (inset). dS/dT is calculated from the smooth curve fits to the $S(T)$ data in figure 4. The shaded regions indicate the temperatures at which a pseudo-gap is inferred from features in the resistivity data below. The open boxes indicate the region of the superconducting transition temperature, T_c , as determined from the vanishing of the resistivity, $\rho(T)$.

samples where there is a sufficient range of data, the value of T^* can be correlated with the region of a broad maximum in dS/dT (an inflection point in $S(T)$) which is moving closer to the value of the transition temperature T_c with increasing x . In the case of the $x = 0.19$ sample the two temperatures T_c and T^* , extracted from resistivity data, coincide as does the corresponding sharp (T_c) and broad (T^*) feature in dS/dT .

For further context, we compare the data here to thermopower measurements on polycrystalline $\text{Sm}_{2-x}\text{Ce}_x\text{CuO}_{4-y}$ and thin films of $\text{Pr}_{2-x}\text{Ce}_x\text{CuO}_{4-y}$. Yang *et al* [29] performed some of the earliest thermopower measurements of polycrystalline $\text{Sm}_{2-x}\text{Ce}_x\text{CuO}_{4-y}$ samples across a wide doping spectrum. In the underdoped limit, the samples were found to have a large negative thermopower voltage, implying n-type carriers. The magnitude of the thermopower voltage decreased as the Ce content was increased until optimal doping at $x = 0.15$ where there was a sign change and a small positive signal (on the

order of $1 \mu\text{V K}^{-1}$) was observed. This small positive signal peaked and then remained at $S \approx 0.5 \mu\text{V K}^{-1}$ up to room temperature. Moving beyond optimal doping ($x > 0.15$), the thermopower voltage retained the same shape as that of the $x = 0.15$ sample; however, there was a sign change at higher temperature with a small magnitude ($S \leq 1 \mu\text{V K}^{-1}$) negative voltage.

More recent thermopower measurements performed by Li *et al* [18] on thin films of $\text{Pr}_{2-x}\text{Ce}_x\text{CuO}_{4-y}$ were observed to be consistent with Hall effect measurements performed on the same samples [30]. It was shown that the sign change in the thermopower was at the same temperature as that of Hall effect measurements, from which the presence of both holes and electrons as charge carriers can be inferred.

The thermopower was observed to have a large negative value for underdoped films, decreasing in magnitude until the $x = 0.16$ overdoped sample, where the thermopower is positive above T_c until $T \approx 25\text{ K}$ where it changes sign. Samples with $x > 0.16$ show a small positive value of S for all temperatures above T_c . These results were taken as evidence for an antiferromagnetic to paramagnetic quantum phase transition in electron-doped cuprates near $x = 0.16$.

The results found here bear some similarities to the results from the thermopower study of polycrystalline $\text{Sm}_{2-x}\text{Ce}_x\text{CuO}_{4-y}$ samples; however, a more consistent comparison can be made to results from $\text{Pr}_{2-x}\text{Ce}_x\text{CuO}_{4-y}$ thin films. One possible reason for the difference is in the nature of the samples themselves, since both thin film studies produced c -axis oriented films and measurements were performed in the ab -plane. The differences with the polycrystalline $\text{Sm}_{2-x}\text{Ce}_x\text{CuO}_{4-y}$ study can likely be attributed to the different orientations of the grains and, possible oxygen inhomogeneities within the grains. However, further comparison of our data with that of the $\text{Pr}_{2-x}\text{Ce}_x\text{CuO}_{4-y}$ thin films show that the only significant difference is the cerium concentration at which there is a sign change in the thermopower. This is observed at optimal doping $x = 0.15$ for $\text{Sm}_{2-x}\text{Ce}_x\text{CuO}_{4-y}$ as opposed to $x = 0.16$ for $\text{Pr}_{2-x}\text{Ce}_x\text{CuO}_{4-y}$. Qualitatively, the data behave as one would expect up to about optimal doping, wherein an increase of the cerium content in the samples should result in a proportional increase in the (electron) carrier concentration. With the thermopower inversely proportional to the carrier concentration, the magnitude of the thermopower is then normally expected to decrease with increased Ce doping. In all of the samples mentioned above, there is a sign change in the measured thermopower voltage as a function of cerium concentration. In both cases, this was explained in terms of a two-band model with a compensation at some critical doping level (x_c), above which the hole contribution dominates. As the data presented here on $\text{Sm}_{2-x}\text{Ce}_x\text{CuO}_{4-y}$ film samples appear to be most consistent with the corresponding data from $\text{Pr}_{2-x}\text{Ce}_x\text{CuO}_{4-y}$ films this would lead us to also invoke a two-band model. This conclusion should be taken in the context of recent quantum oscillation experiments on the electron doped superconductor $\text{Nd}_{2-x}\text{Ce}_x\text{CuO}_{4-y}$ [31] and on hole-doped high- T_c cuprates, which have been interpreted as evidence for two conduction bands at the Fermi surface consisting of both holes [32] and electrons [33, 34]. The possible existence of

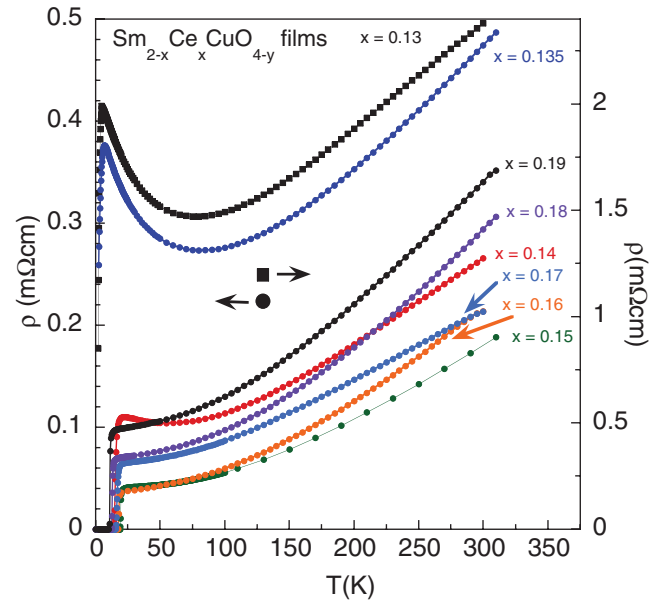


Figure 6. Resistivity $\rho(T)$ in zero magnetic field for thin film samples of $\text{Sm}_{2-x}\text{Ce}_x\text{CuO}_{4-y}$ with $x = 0.13$ – 0.19 .

two-band superconductivity in both hole- and electron-doped cuprates suggests an important electronic commonality in spite of other known differences in their electronic structures and superconducting phase diagrams.

3.2. Electrical transport measurements

3.2.1. $H - T_c - x$ phase diagram. Measurements of resistivity ρ versus temperature in zero magnetic field of all samples are shown in figure 6. The superconducting transition temperature T_c for each of the films, shown in figure 10, was taken as the temperature at which the resistivity drops to 50% of the normal state value at temperatures just above the transition. The transition width, ΔT_c , is taken as the difference in temperature between the 10%–90% drop in the normal state resistivity values. The values of the critical temperatures determined by the mid point transition $T_c(\text{K})_{(\text{mid})}$ for all samples are given in table 1.

Resistivity $\rho(T)$ measurements in fixed magnetic fields up to 9 T were performed on each $\text{Sm}_{2-x}\text{Ce}_x\text{CuO}_{4-y}$ film. In figure 7 we show $\rho(T)$ data for the $x = 0.17$ sample. As more easily seen in the inset, as superconductivity is suppressed by increasing the magnetic field, the resistivity begins to exhibit a clear upturn at low temperatures. This upturn is observed in the high field $\rho(T)$ data of each sample. As shown in figure 6, the zero field resistivity data of the underdoped samples already exhibit such an upturn, prior to the transition into the superconducting state. Interestingly though, we find that the high field data ($H \geq 7\text{ T}$) for all samples, underdoped to overdoped, can be fit well to an empirical expression $\rho(T) = \rho_0 + a/T + bT + cT^2$ from $T = 2\text{ K}$ (the lowest temperatures measured) up to temperatures well above ($40\text{ K} \leq T \leq 160\text{ K}$) the critical temperature T_c . The low temperature-high field behavior observed here across the doping range $x = 0.13$ – 0.19 of $\text{Sm}_{2-x}\text{Ce}_x\text{CuO}_{4-y}$ is in marked

Table 1. Values of the superconducting critical temperature at the midpoint of the transition and at the vanishing of the resistivity, $T_c(\text{K})_{(\text{mid})}$ and $T_c(\text{K})_{(\rho \rightarrow 0)}$, respectively, the superconducting transition width, ΔT_c , the pseudogap temperature T^* , the critical exponent $s \equiv \nu(z - 1)$, and the estimated error of s , Δs , for each Ce concentration x .

x	$T_c(\text{K})_{M(T)}$	$T_c(\text{K})_{(\rho \rightarrow 0)}$	$T_c(\text{K})_{(\text{mid})}$	$\Delta T_c(\text{K})$	$T^*(\text{K})$	s	Δs
0.13	—	~ 1.2	~ 2	—	55	—	—
0.135	—	~ 1.5	~ 2	—	—	—	—
0.14	14.7	14.0	15.4	2.5	—	2.11	0.15
0.15	17.5	19.0	19.5	0.6	42	2.60	0.25
0.16	15.5	17.4	18.0	0.9	30	2.45	0.25
0.17	13.3	15.4	16.7	1.9	24	2.60	0.25
0.18	7.5	12.4	12.9	1.1	15.5	2.33	0.1
0.19	7.0	10.8	11.2	0.9	10.5	2.45	0.2

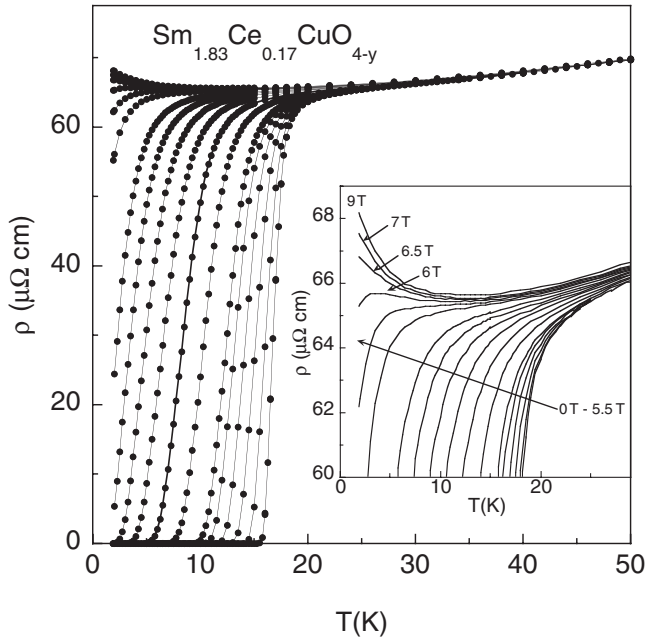


Figure 7. Resistivity $\rho(T)$ in magnetic fields up to 9 T for the $x = 0.17$ sample. The data shown are taken in magnetic fields of 0 T to 0.8 T in 0.2 T increments, 1.0 T to 7 T in 0.5 T increments, and at 9 T. Additional $\rho(H)$ versus T data were taken at other fields not shown here.

contrast to that found for the electron doped cuprate systems $\text{La}_{2-x}\text{Ce}_x\text{CuO}_4$ and $\text{Pr}_{2-x}\text{Ce}_x\text{CuO}_{4-y}$, where an insulator-to-metal transition is observed to occur near optimal doping via resistivity measurements in large magnetic fields [35–37]. At a concentration of $x = 0.17$ the high field resistivity $\rho(T)$ of $\text{La}_{2-x}\text{Ce}_x\text{CuO}_4$ and $\text{Pr}_{2-x}\text{Ce}_x\text{CuO}_{4-y}$ monotonically decreases to a residual value with a $\rho(T) \sim T^n$ dependence with $n > 1$ and $n = 1$ respectively. It would appear that the persistence of an insulating-like component in the resistivity $\rho(T)$ in samples with Ce concentrations up to at least $x = 0.19$ is unique to the $\text{Sm}_{2-x}\text{Ce}_x\text{CuO}_{4-y}$ system. We note that for both the $\text{La}_{2-x}\text{Ce}_x\text{CuO}_4$ and $\text{Pr}_{2-x}\text{Ce}_x\text{CuO}_{4-y}$ systems, the characteristic temperature $T_{\text{min}}(x)$, corresponding to an observed local minimum in the $\rho_{ab}(T)$ ($H = 0$) data, vanishes in the vicinity of $x = 0.15$ [37, 38]. The temperature $T_{\text{min}}(x)$ is frequently taken as being indicative of the presence of the pseudogap, where $T_{\text{min}}(x) \leq T^*(x)$.

In figures 8 and 9, we show analyses of the resistivity data of the $\text{Sm}_{2-x}\text{Ce}_x\text{CuO}_{4-y}$ films from which we infer temperature

T^* of the proposed pseudogap for each film, excluding the $x = 0.135$ and 0.14 samples. For the $x = 0.16$ – 0.19 samples, $T^*(x)$ is determined by the temperature at which a distinct ‘kink’ is observed when the constant ρ_0 and T^{-1} terms are subtracted from the high field ($H = 9\text{T}$) resistivity versus temperature data, i.e. $\rho(T) - (\rho_0 + a/T)$. This feature is clearly visible for the $x = 0.17$ and $x = 0.19$ samples. For the $x = 0.18$ sample we have also plotted (figure 9(b) inset) $d\{\rho(T) - (\rho_0 + a/T)\}/dT$ versus T wherein the ‘kink’ is more pronounced.

As noted above, all of the $\text{Sm}_{2-x}\text{Ce}_x\text{CuO}_{4-y}$ films that we have grown are subject to a shelf life that limits the time period over which measurements can be performed. Unfortunately, the high field data of the $x = 0.13$ – 0.15 samples do not extend to temperatures high enough by which we can perform the same analysis as done for the $x = 0.16$ – 0.19 films. Since these films have since exceeded their shelf life, further measurements can not be performed. However, we find that we can extract meaningful values for T^* for the $x = 0.13$ and $x = 0.15$ samples through the following procedure: for the $x = 0.13$ sample, we observe at low temperatures (still above T_c) a negative magnetoresistive response that decreases in magnitude as temperature is increased. This behavior is similar to the $\rho_c(T)$ data taken in various magnetic fields by Kawakami on single crystals of $\text{Sm}_{2-x}\text{Ce}_x\text{CuO}_{4-y}$ from which the pseudogap temperature for this system was inferred in the doping range $0.14 \leq x \leq 0.156$ by the temperature at which a negative magnetoresistance was observed, increasing in magnitude to lower temperatures [9]. It seems likely that, due to some roughness of the sample surface, the measured resistivity of this film contains a small ρ_c component, to which we attribute the observed negative magnetoresistance. The in field resistivity $\rho(T)$ data taken here does not extend to a temperature high enough to directly determine T^* by the point at which the zero field and high field data merge; however, we obtain a reasonable estimate by an extrapolation of the data as shown in the inset of figure 8(a). For the $x = 0.15$ sample, we have determined an estimate for T^* by extrapolating the 9 T $\rho(T)$ data to higher temperatures, and by the location of an inflection point observed in the ($H = 0$) $\rho(T)$ data (figure 8(b)). The values for $T^*(x)$ determined here are given in table 1, and shown in figure 10 along with the data of Kawakami *et al* [10].

From the above zero field and high field $\rho(T)$ data, we construct in figure 10 a temperature T versus Ce concentration x phase diagram. Our results for T_c are found to be comparable to a recent $T_c - x$ phase diagram constructed by

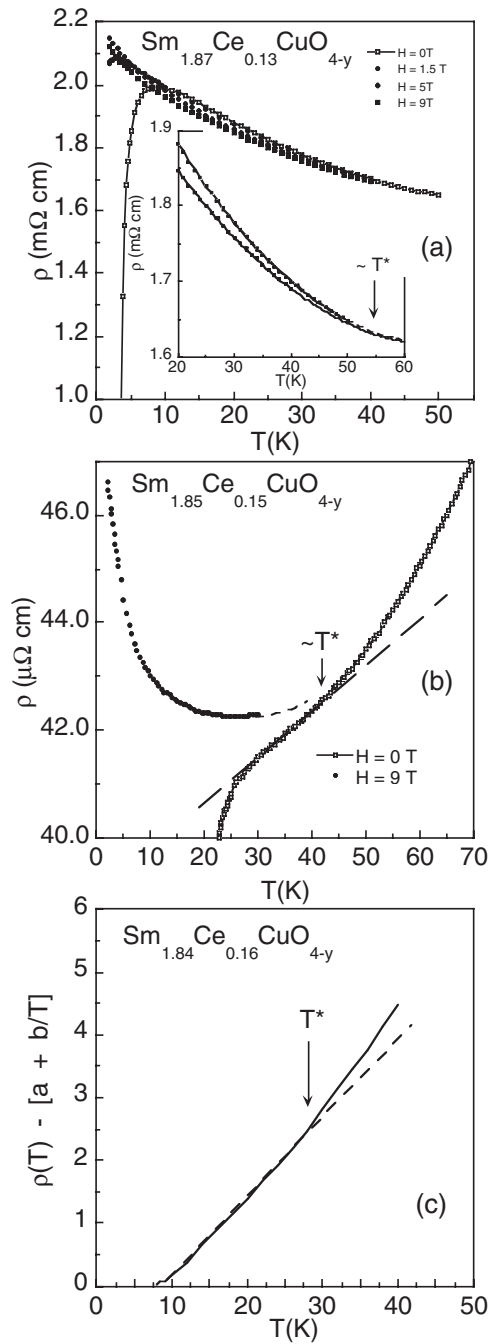


Figure 8. In field ($H = 9$ T) resistivity data from which the pseudogap temperature T^* is inferred for $\text{Sm}_{2-x}\text{Ce}_x\text{CuO}_{4-y}$ thin film samples $x = 0.13, 0.15$ and 0.16 . See the text for further explanation of the criteria by which T^* was established.

Krockenberger *et al* [8], for MBE-grown epitaxial thin films of $\text{Sm}_{2-x}\text{Ce}_x\text{CuO}_{4-y}$. There is good agreement between the transition temperatures T_c of samples in the $x = 0.15-0.17$ range produced from both growth methods. There is also good agreement as to the Ce concentration in the underdoped region at which superconductivity emerges—in the range of $x \approx 0.125$ (here) to $x \approx 0.13$ (MBE-films). However, there appears to be a disagreement as to the temperature in the overdoped region at which the superconducting dome terminates. We obtain higher values of T_c for $x \geq 0.18$, resulting in an *extrapolated* critical upper concentration of $x \approx 0.22$ that is

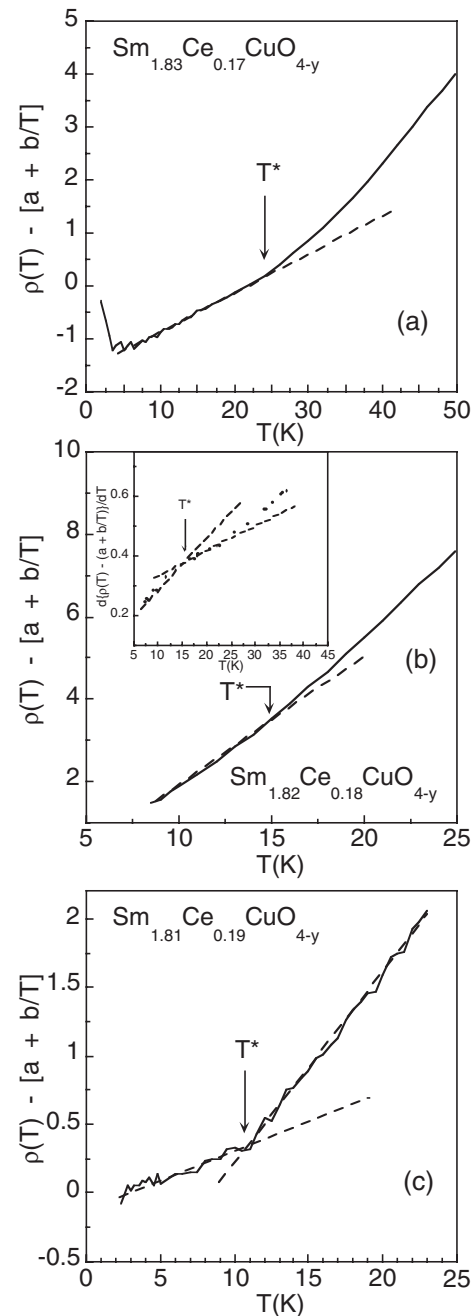


Figure 9. In field ($H = 9$ T) resistivity data from which the pseudogap temperature T^* is inferred for $\text{Sm}_{2-x}\text{Ce}_x\text{CuO}_{4-y}$ thin film samples $x = 0.17, 0.18$ and 0.19 . See the text for further explanation of the criteria by which T^* was established.

somewhat higher than that of the experimentally determined value of $x \approx 0.21$ for the MBE-films. In either case, this places the termination of the linearly extrapolated $T^* - x$ line, ($T^* = 0$ K), at $x \approx 0.20$, i.e. within the superconducting ‘dome.’ This result is relevant in the context of the many competing scenarios as to the relationship of the purported pseudogap phase to the superconducting state [39, 40].

3.2.2. Vortex-glass scaling analysis. From the above in field $\rho(T)$ measurements the vortex-solid to vortex-liquid transition boundary, shown in figure 11, was determined for samples with $0.14 \leq x \leq 0.19$. The shape of this boundary

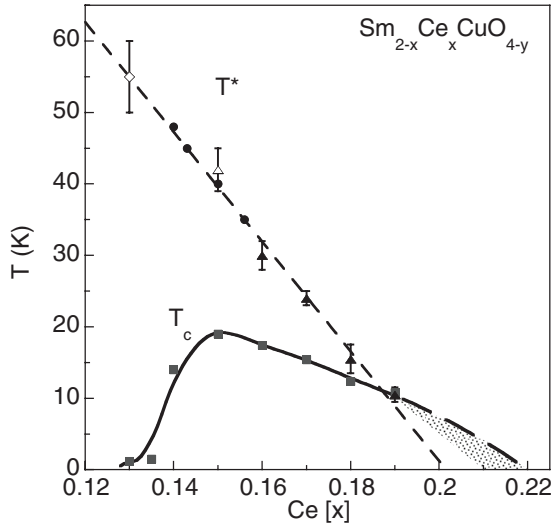


Figure 10. Superconducting transition temperature T_c (squares) versus cerium concentration, x , for $\text{Sm}_{2-x}\text{Ce}_x\text{CuO}_{4-y}$ thin film samples with $x = 0.13$ to $x = 0.19$. The solid line is a guide to the eye. Also shown is the pseudogap temperature T^* versus x as determined from analysis of the resistivity data of the $\text{Sm}_{2-x}\text{Ce}_x\text{CuO}_{4-y}$ films (closed triangles, open triangle, open diamond) as indicated in figures 8 and 9, and as determined by Kawakami *et al* [10], from c -axis electrical transport measurements performed on $\text{Sm}_{2-x}\text{Ce}_x\text{CuO}_{4-y}$ single crystals (circles). The dashed line is a linear fit to the T^* data. The shaded section indicates the region over which there is a possible difference between the T_c versus x result found here and that found for MBE-grown films [8] as described in the text.

in the underdoped region has an upward curvature with decreasing temperature that is typically reported for high- T_c compounds [41]. However, as the system progresses into the overdoped region, the $H_g(T)$ line rapidly loses this steep upward curvature, developing a form approaching that of the upper critical field $H_{c2}(T)$ of a conventional BCS two-band superconductor [42].

The observed evolution of the field-temperature ($H - T$) dependence of the vortex glass melting line, $H_g(T)$, has previously been examined for $\text{Sm}_{2-x}\text{Ce}_x\text{CuO}_{4-y}$ films as well as hole-doped high- T_c cuprate $\text{Y}_{0.8}\text{Ca}_{0.2}\text{Ba}_2\text{Cu}_3\text{O}_x$ films [43] in the context of the modified quantum-thermal fluctuation vortex-lattice melting theory [44, 45] of Blatter and Ivlev [46]. Blatter and Ivlev included the contribution of quantum fluctuations to the statistical mechanics of the vortex-solid to vortex-liquid transition. In [43] a connection between the relative strength of quantum to thermally driven vortex fluctuations, as characterized by a quantum fluctuation parameter Q , [44], (or q , [45]) and the sharp upturn of $H_g(T)$ as a function of charge doping was demonstrated for both compounds. It was proposed that the pseudo-gap was responsible for the strength of quantum fluctuations—being that the dominant population of quasiparticles in the vortex core likely belong to the pseudo-gap, rather than being Drude-type. Such an interpretation would be consistent with the results here interpreting the correlation of the temperature, $T^*(x)$, at which linear feature in the resistivity appears, and the temperature region of a broad maximum in dS/dT as attributable to a pseudo-gap.

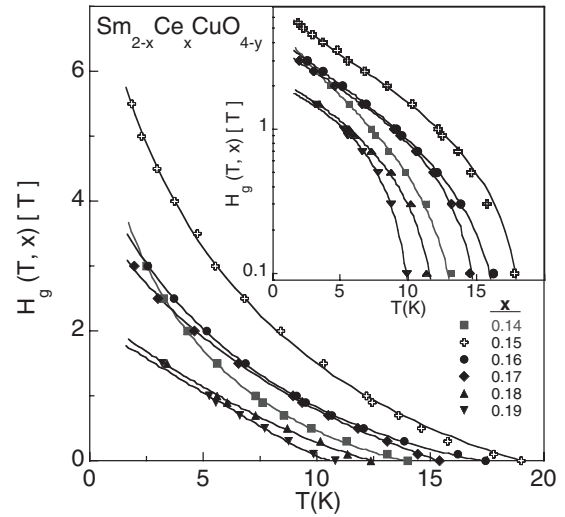


Figure 11. Vortex glass melting lines, $H_g(T)$, determined via analysis in the context of the RRA model, for each cerium concentration x , with $x = 0.14$ to $x = 0.19$. Inset: same data as in the main panel, plotted on a semi-log scale. The solid curves shown are fits to the data by the empirical expression for the vortex glass melting line found in [44], as reported in [43]. Values of the fitting parameters can also be found in [43].

However, with respect to the upturn of $H_g(T)$ in the underdoped regime, an alternate scenario has been proposed by Cooper *et al*, that attributes the increase in $H_g(T)$ at low T as arising from the enhancement of thermal fluctuations by a weakening of the superconducting condensate by a magnetic field [47]. A condition is proposed wherein the predicted effect will be significant for any material for which $U\Omega < \sim k_B T_c$, but that effects could still be observed for $U\Omega \sim 10 k_B T_c$. $U\Omega$ is the condensation energy per coherence volume in zero field. In [48], from an extension of the expression of the vortex glass melting line arrived at in [44], a relationship between T_c and the condensation energy density was found where, $k_B T_c = 8\pi\sqrt{2}(\pi^2 c_L^4)^\alpha (H_c^2/2\mu_0)V_{\text{coh}}$. c_L is the Lindemann melting-criterion parameter and α is an exponent describing the curvature of $H_g(T)$ [45, 48]. In [43] average values of $c_L \approx 0.23$ and $\alpha \approx 2.0$ were found for $\text{Sm}_{2-x}\text{Ce}_x\text{CuO}_{4-y}$ films with Ce concentrations $0.14 \leq x \leq 0.18$. A value of $\alpha \approx 3.7$ was found for $x = 0.19$. Using these values we then have $(H_c^2/2\mu_0)V_{\text{coh}} \approx (36.9) k_B T_c$ for $0.14 \leq x \leq 0.18$, and $(H_c^2/2\mu_0)V_{\text{coh}} \approx (16\,500) k_B T_c$ for $x = 0.19$. These results suggest that within the range of $0.14 \leq x \leq 0.18$ the $\text{Sm}_{2-x}\text{Ce}_x\text{CuO}_{4-y}$ system is at, or just beyond, the upper limit of meeting the criterion for the proposed magnetic field enhancement of thermal fluctuations, and that the $x = 0.19$ sample (where the purported pseudo-gap terminates [43]) falls well outside. This is not to say though that physical mechanism behind of the proposition of Cooper *et al* is not relevant or valid. A similar approach incorporating the relevance of the strength of a pinning energy scale $U_0(B, T_g)$, to the temperature in determining the vortex-solid to vortex-liquid transition, where the transition occurs when $U_0(B, T_g) = k_B T_g$, was introduced by Rydh, Rapp, and Andersson (RRA) [49, 50]. In turn, the modified vortex glass theory of RRA is an extension of the vortex-glass model of Fisher–Fisher–Huse (FFH) [51]. It seems reasonable

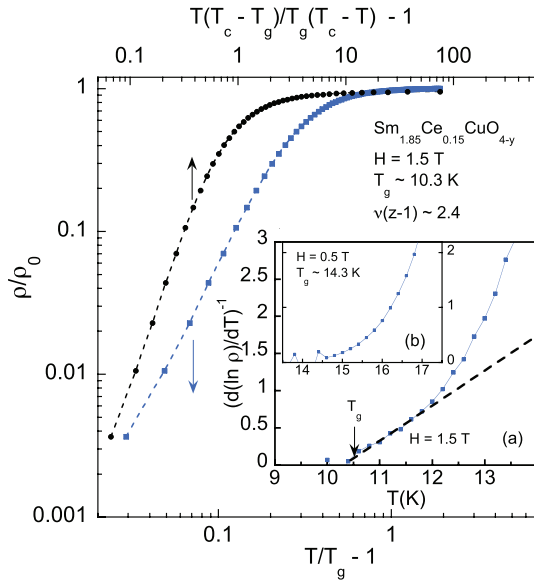


Figure 12. (main panel) Normalized resistivity data versus the FFH and RRA temperature scaling forms, plotted on a double x-axis for the optimally doped $\text{Sm}_{1.85}\text{Ce}_{0.15}\text{CuO}_{4-y}$ sample with $H = 1.5$ T. (a) Scaled resistivity $d \ln \rho/dT$ versus T for the same data in the main panel. The dark line is a guide to the eye through the region to which a linear fit was applied. (b) Scaled resistivity $d \ln \rho/dT$ versus T for the same sample with $H = 0.5$ T. A clear linear region is not identifiable.

to consider that magnetic field enhanced thermally-driven fluctuations of the condensate, as proposed by Cooper *et al*, are compatible with the magnetic field and temperature dependence of the pinning energy proposed by RRA. Furthermore, the model of RRA can be shown to be a high q limiting case of the modified quantum-thermal vortex-lattice melting theory [44, 45]. The various connections between these theories highlights both the complexity of the physics at play as well as the compatibility of the proposed relevant physical mechanisms.

The magnetoresistance data were further analyzed in the context of the Fisher–Fisher–Huse (FFH) vortex glass scaling model [51], as well as the modified vortex glass model of Rydh, Rapp, and Andersson (RRA) [49, 50]. As shown below we find the data is better represented by the RRA modified vortex glass expressions. In the critical region, at temperatures above the vortex glass melting temperature T_g , the resistivity conforms to an equation of the form: $\rho = \rho_0 |T/T_g - 1|^{\nu(z+2-d)}$. Assuming $d = 3$ then gives: $\rho = \rho_0 |T/T_g - 1|^{\nu(z-1)}$. When performing an analysis of in field resistivity data in the context of the FFH model, a plot of $(d \ln \rho/dT)^{-1}$ versus T , is used to clearly identify a region of linear behavior – corresponding to the critical region of the vortex glass melting transition—from which the values of T_g and $\nu(z - 1)$ can be extracted. (See for instance figure 2 of [45] or figure 3 of [50] for FFH scaling of resistivity data for $\text{YBa}_2\text{Cu}_3\text{O}_{7-\delta}$ samples). This scaling analysis was performed on the data here for each magnetic field applied to the samples with cerium concentration $x \geq 0.14$. A plot of $(d \ln \rho/dT)^{-1}$ versus T for the $\text{Sm}_{1.85}\text{Ce}_{0.15}\text{CuO}_{4-y}$ sample with $H = 1.5$ T is shown in inset (a) of figure 12 with a linear fit shown to a region of the data. It can be seen that a region of linearly vanishing data is not as readily apparent as

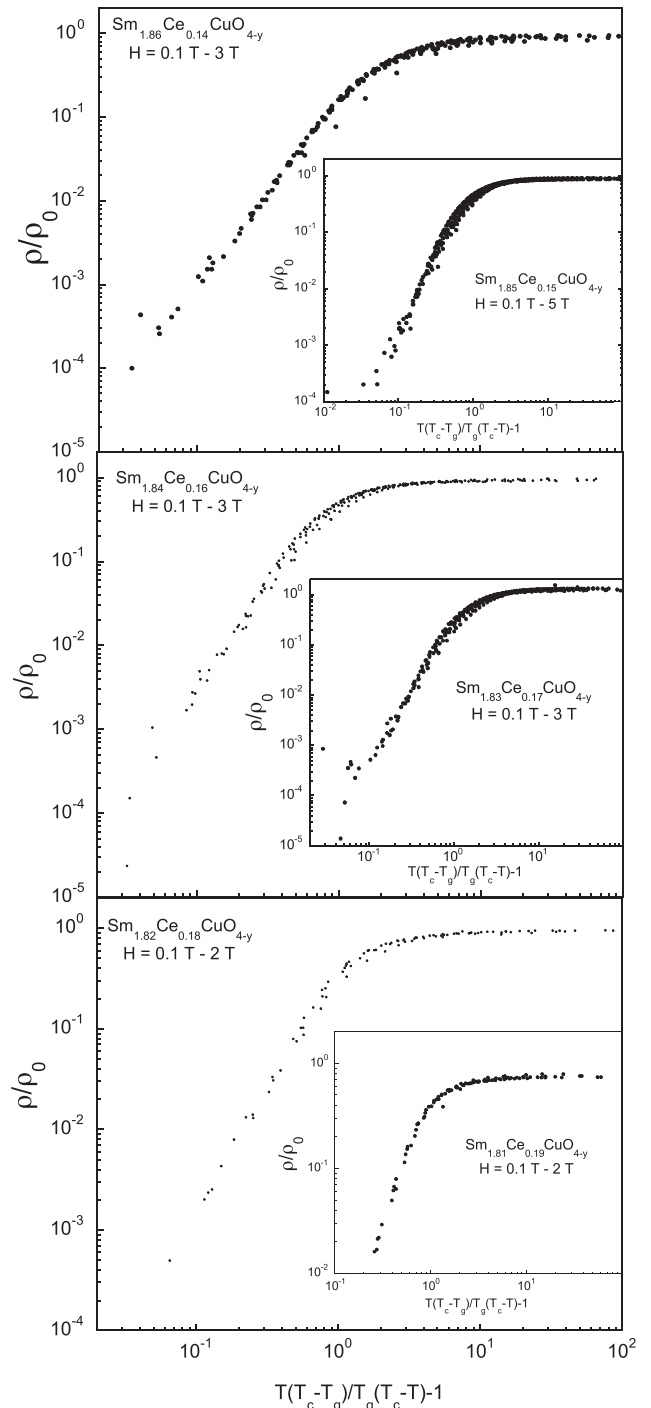


Figure 13. Resistivity data scaled according to the expression given in equation (1) for samples with cerium concentrations between $x = 0.14$ and $x = 0.19$.

what is generally reported [45, 50]. As a further example, in inset (b) we show a plot of $(d \ln \rho/dT)^{-1}$ versus T for $H = 0.5$, where arguably no linear region is evident. These results are typical of all the $H_g(T)$ data analyzed in this manner, suggesting that the original FFH vortex glass melting transition scenario may not be adequate for describing the vortex-solid to vortex-liquid transition of the $\text{Sm}_{2-x}\text{Ce}_x\text{CuO}_{4-y}$ system. For further comparison we show in the main panel of figure 12 the normalized resistivity data of the same data in the inset

plotted on a double x -axis versus the FFH and RRA vortex glass scaling of the temperature as shown on the lower and upper axes, respectively. From such a plot, it is not readily straightforward from this to establish which model provides a better description of the data, however, as shown below, the RRA scaling method does provide a consistent means to uniformly scale the resistivity data for the entire vortex glass line of each sample in a way the FFH model does not.

From the model proposed by RRA, a modified scaling expression for the resistivity in the critical region is obtained such that,

$$\rho(T) = \rho_0 \left| \frac{T(T_c - T_g)}{T_g(T_c - T)} - 1 \right|^{\nu(z-1)}, \quad (1)$$

where ρ_0 is taken as the normal state resistivity just above T_c . The RRA model differs from the FFH model in that the authors claim that the pinning energy scale changes with both temperature and magnetic field such that the vortex glass transition is dependent on the energy difference $k_B T - U_0(H, T)$, where U_0 is the current independent mean pinning energy. Qualitatively speaking, this can be thought of in terms of using the two dimensional distance in the $H - T$ plane to traverse to T_g , instead of taking the usual one dimensional distance in temperature to T_g at a constant field H . By plotting ρ/ρ_n versus $(T(T_c - T_g)/T_g(T_c - T) - 1)$ on a log-log plot, the resistivity data taken in various fixed fields should collapse onto a single curve, from which a value for T_g and $\nu(z - 1)$ can be obtained. The modified scaling expression given in equation (1) was very successful in accurately describing the data. The data for all of the concentrations in this study also scale according to this relation and this is shown in the plots in figure 13. Although both scaling models give results that are reasonably consistent with respect to the value of the critical temperature T_g , the temperature range over which the data could be fit to the expression from the RRA scaling model was much clearer than that of the expression from the FFH model. As such, there was much less uncertainty in the values of $\nu(z - 1)$ obtained from the RRA model. Values of the exponent $\nu(z - 1)$ obtained via the RRA scaling analysis are given in table 1. The significantly better fits to the data from the RRA model lead us to conclude that, for the $\text{Sm}_{2-x}\text{Ce}_x\text{CuO}_{4-y}$ system, the melting of the solid vortex state is significantly influenced by the effects of the magnetic field on the pinning landscape. While it is tempting to attribute this finding to the presence of the Sm sublattice, it is not readily discernible as to whether or not this unusual behavior can be attributed to an interaction of the flux line lattice with the Sm^{3+} ions. However, since the Néel temperature $T_N \sim 6$ K of the Sm sublattice is below that of the majority of the length of the $H_g(T)$ lines, the antiferromagnetic ordering of the Sm^{3+} ions (in the ab-plane) would seem to play no significant role in the dynamical properties of vortices in the region of the melting transition.

4. Concluding remarks

Electrical transport measurements were performed on high quality PLD grown epitaxial $\text{Sm}_{2-x}\text{Ce}_x\text{CuO}_{4-y}$ films, from which we have developed further the $H - T - x$ phase

diagram of this electron-doped high- T_c superconductor. We find a $T_c - x$ region in good agreement with that found for MBE grown $\text{Sm}_{2-x}\text{Ce}_x\text{CuO}_{4-y}$ films [8], with the notable difference of higher T_c values obtained in the overdoped region, and subsequently a slight extension of the T_c region to a higher Ce doping level was inferred by us. From an analysis of the in-plane resistivity $\rho_{ab}(T)$ in high magnetic fields we have extended the doping range over which the proposed pseudogap line $T^*(x)$ has been previously determined [10]. The evolution of the boundary between the solid and liquid vortex phases, $H_g(T)$, was examined for samples with $0.14 \leq x \leq 0.19$ and can be seen to develop towards a form in the overdoped region consistent with the upper critical field $H_{c2}(T)$ of a two-band BCS superconductor [42]. The possible existence of two superconducting bands in $\text{Sm}_{2-x}\text{Ce}_x\text{CuO}_{4-y}$ is further supported by thermopower measurements presented here that are strikingly similar to those obtained on $\text{Pr}_{2-x}\text{Ce}_x\text{CuO}_{4-y}$ films [18], which, in conjunction with Hall effect measurements, have been cited as evidence supportive of this picture. Finally, from a scaling analysis of the vanishing of the resistivity $\rho(T)$ along the $H_g(T)$ boundary, we find evidence for an appreciable effect of the applied field on the pinning landscape of the vortex flux line lattice.

Acknowledgments

The research at UCSD was supported by the U.S. Department of Energy, Office of Basic Energy Sciences, Division of Materials Sciences and Engineering under Grant No. DE-FG02-04ER46105 (sample synthesis) and the National Science Foundation under Grant No. DMR-1206553 (sample characterization). A portion of this work was performed at the National High Magnetic Field Laboratory, which is supported by NSF Cooperative Agreement No. DMR-0084173, by the State of Florida, and by the DOE.

References

- [1] Armitage N P, Fournier P and Greene R L 2010 *Rev. Mod. Phys.* **82** 2421
- [2] Rotundu C R, Struzhkin V V, Somayazulu M S, Sinogeikin S, Hemley R J and Greene R L 2013 *Phys. Rev. B* **87** 024506
- [3] Kunwar S 2014 *J. Supercond. Novel Magn.* **27** 2461
- [4] Zeng S W *et al* 2015 *Phys. Rev. B* **92** 020503
- [5] da Silva Neto E H, Comin R, He F, Sutarto R, Jiang Y, Greene R L, Sawatzky G A and Damascelli A 2015 *Science* **347** 282
- [6] Saadaoui H *et al* 2015 *Nat. Commun.* **6** 1
- [7] Zhanga X, Yua H, Hea G, Hua W, Yuana J, Zhua B and Jin K 2016 *Physica C* **525-6** 18
- [8] Krockenberger Y, Kurian J, Winkler A, Tsukada A, Naito M and Alff L 2008 *Phys. Rev. B* **77** 060505
- [9] Kawakami T, Shibauchi T, Terao Y, Suzuki M and Krusin-Elbaum L 2005 *Phys. Rev. Lett.* **95** 017001
- [10] Kawakami T, Shibauchi T, Terao Y and Suzuki M 2006 *Phys. Rev. B* **74** 144520
- [11] Park S R, Roh Y S, Yoon Y K, Leem C S, Kim J H, Kim B J, Koh H, Eisaki H, Armitage N P and Kim C 2007 *Phys. Rev. B* **75** 060501
- [12] Zimmers A, Noat Y, Cren T, Sacks W, Roditchev D, Liang B and Greene R L 2007 *Phys. Rev. B* **76** 132505

- [13] Ikeda M, Yoshida T, Fujimori A, Kubota M, Ono K, Das H, Saha-Dasgupta T, Unozawa K, Kaga Y, Sasagawa T and Takagi H 2009 *Phys. Rev. B* **80** 014510
- [14] Korshunov M M, Zakharova E V, Nekrasov I A, Pchelkina Z V and Ovchinnikov S G 2010 *J. Phys.: Condens. Matter* **22** 015701
- [15] Sumarlin I W, Skanthakumar S, Lynn J W, Peng J L, Li Z Y, Jiang W and Greene R L 1992 *Phys. Rev. Lett.* **68** 2228
- [16] Wilson S D, Dai P, Li S, Chi S, Kang H J and Lynn J W 2006 *Nature* **442** 59
- [17] Wilson S D, Li S, Woo H, Dai P, Mook H A, Frost C D, Komiya S and Ando Y 2006 *Phys. Rev. Lett.* **96** 157001
- [18] Li P, Behnia K and Greene R L 2007 *Phys. Rev. B* **75** 020506
- [19] Krasnov V M, Yurgens A, Winkler D, Delsing P and Claeson T 2000 *Phys. Rev. Lett.* **84** 5860
- [20] Sonier J E et al 2001 *Science* **292** 1692
- [21] Xia J et al 2008 *Phys. Rev. Lett.* **100** 127002
- [22] Daou R et al 2009 *Nat. Phys.* **5** 31
- [23] Gor'kov L P and Teitel'baum G B 2006 *Phys. Rev. Lett.* **97** 247003
- [24] Fujita M, Matsuda M, Lee S-H, Nakagawa M and Yamada K 2008 *Phys. Rev. Lett.* **101** 107003
- [25] Scalapino D J 2012 *Rev. Mod. Phys.* **84** 1383
- [26] Jin K, Hu W, Zhu B, Kim D, Yuan J, Sun Y, Xiang T, Fuhrer M S, Takeuchi I and Greene R L 2016 *Sci. Rep.* **6** 26642
- [27] Early E A 1991 *PhD Thesis* University of California, San Diego
- [28] Kang H J, Dai P, Campbell B J, Chupas P J, Rosenkranz S, Lee P L, Huang Q, Li S, Komiya S and Ando Y 2007 *Nat. Mater.* **6** 224
- [29] Yang H S, Chai Y S, Liu J, Yu M, Li P C, Zhang L, Li M D and Cao L Z 2004 *Physica C* **403** 203
- [30] Dagan Y, Qazilbash M M, Hill C P, Kulkarni V N and Greene R L 2004 *Phys. Rev. Lett.* **92** 167001
- [31] Helm T, Kartsovnik M V, Bartkowiak M, Bittner N, Lambacher M, Erb A, Wosnitza J and Gross R 2009 *Phys. Rev. Lett.* **103** 157002
- [32] Sebastain S E, Harrison N, Palm E, Murphy T P, Mielke C H, Liang R, Bonn D A, Hardy W N and Lonzarich G G 2008 *Nature* **454** 200
- [33] Doiron-Leyraud N, Proust C, LeBoeuf D, Levallios J, Bonnemaïson J-B, Liang R, Bonn D A, Hardy W N and Taillefer L 2007 *Nature* **447** 565
- [34] LaBoeuf D et al 2007 *Nature* **450** 533
- [35] Boebinger G S, Ando Y, Passner A, Kimura T, Okuya M, Shimoyama J, Kishio K, Tamasaku K, Ichikawa N and Uchida S 1996 *Phys. Rev. Lett.* **77** 5417
- [36] Jin K, Zhu B Y, Wu B X, Vanacken J, Moshchalkov V V, Xu B, Cao L X, Qiu X G and Zhao B R 2008 *Phys. Rev. B* **77** 172503
- [37] Fournier P, Mohanty P, Maiser E, Darzens S, Venkatesan T, Lobb C J, Czjzek G, Webb R A and Greene R L 1998 *Phys. Rev. Lett.* **81** 4720
- [38] Wu B X, Jin K, Yuan J, Wang H B, Hatano T, Zhao B R and Zhu B Y 2009 *Physica C* **469** 1945
- [39] Timusk T and Statt B 1999 *Rep. Prog. Phys.* **62** 61
- [40] Norman M R, Pines D and Kallin C 2005 *Adv. Phys.* **54** 715
- [41] Maple M B et al 1994 *J. Supercond.* **7** 97
- [42] Mansor M and Carbotte J P 2005 *Phys. Rev. B* **72** 024538
- [43] Taylor B J, Baumbach R E, Scanderbeg D J and Maple M B 2010 *Phys. Rev. B* **81** 174511
- [44] Taylor B J and Maple M B 2007 *Phys. Rev. B* **76** 014517
- [45] Taylor B J, Scanderbeg D J, Maple M B, Kwon C and Jia Q X 2007 *Phys. Rev. B* **76** 014518
- [46] Blatter G and Ivlev B 1993 *Phys. Rev. Lett.* **70** 2621
- [47] Blatter G and Ivlev B I 1994 *Phys. Rev. B* **50** 10272
- [48] Cooper J R, Loram J W and Wade J M 1995 *Phys. Rev. B* **51** 6179
- [49] Taylor B J and Maple M B 2007 *Phys. Rev. B* **76** 184512
- [50] Rydh A, Rapp Ö and Andersson M 1992 *Phys. Rev. Lett.* **83** 1850
- [51] Andersson M, Rydh A and Rapp Ö 2001 *Phys. Rev. B* **63** 184511
- [52] Fisher D S, Fisher M P A and Huse D A 1991 *Phys. Rev. B* **43** 130